We are IntechOpen, the world's leading publisher of Open Access books Built by scientists, for scientists

4,800
Open access books available

122,000
International authors and editors

135M
Downloads

Our authors are among the

154
Countries delivered to

TOP 1%
most cited scientists

12.2%
Contributors from top 500 universities

WEB OF SCIENCE™

Selection of our books indexed in the Book Citation Index in Web of Science™ Core Collection (BKCI)

Interested in publishing with us?
Contact book.department@intechopen.com

Numbers displayed above are based on latest data collected.
For more information visit www.intechopen.com

5

Simulation of Flow Control with Microjets for Subsonic Jet Noise Reduction

Maxime Huet, Gilles Rahier and François Vuillot
Onera – The French Aerospace Lab, F-92322 Châtillon
France

1. Introduction

With the increasing flight traffic in the past years grew up several types of pollutions for all near airports inhabitants. One of those major pollutions is the noise generated by aircrafts at takeoff. Despite all the work performed during the last decades on the understanding of the noise generation and its reduction, this nuisance still remains a really challenging problem. Above all the noise sources on a plane during takeoff, jet noise remains the dominant one, justifying all the efforts still performed on the topic.

For subsonic jets, radiated noise is a consequence of flow mixing. It is now universally admitted that this mixing noise is generated by the turbulence of the flow and that the noise producing region is axially restricted to about two potential core lengths (Fisher et al., 1977; Laufer et al., 1976). Turbulence is separated in this region in small turbulent eddies, with small dimensions compared to the nozzle, and large-scale structures. It is especially confirmed by the experimental observations (Tam et al., 2008) that both fine- and large-scale structures are the noise sources, large turbulent eddies being predominant in downstream direction especially for high speed jets.

Based on these observations, noise reduction devices are designed to act on jet turbulence development and especially to decrease the growth of the large scale structures in order to reduce major noise generation mechanisms. Several passive and active processes such as chevrons (Bridges & Brown, 2004; Nesbitt & Young, 2008) and microjets are currently being investigated experimentally and numerically. A major advantage of microjets, compared to passive devices, is their possibility to be turned off during cruise, which limits the thrust loss to takeoff configuration only, for instance.

The use of continuous air microjets on Mach 0.9 high Reynolds round jets has been experimentally investigated in the recent years (Alkislar et al., 2007; Arakeri et al., 2003; Castelain, 2006; Castelain et al., 2007; 2008). Measured data show that the interaction between each actuator and the jet shear layer corrugates the main flow over a distance of two to three jet diameters after the nozzle exit and generates a pair of counter-rotating axial vortices downstream of each microjet. All authors also observed a reduction of turbulence intensities in the shear layer and a lengthening of the potential core, with the exception of Alkislar et al. who noticed a turbulence increase 2 jet diameters after the nozzle exit, before its reduction downstream. In the far field, sound is decreased by 0.5 dB to 2 dB for all observation angles, which corresponds to low and medium frequency spectra reductions originating from the collapse of large turbulent structures. Higher frequency levels are increased by the microjets; this high frequency lift is explained by the enhancing of the small-scale structures by the fluid

injection. Such turbulence modifications and related noise variations are similar to what is observed with chevrons, for instance (Alkislar et al., 2007).

A more important noise reduction up to 6 dB has been observed using water injection (Krothapalli et al., 2003), which did not exhibit high frequency lift. From these observations, Zaman (Zaman, 2010) suggests that this high frequency crossover is at least partly due to microjets self noise. Water injection nevertheless remains difficult to use on airplanes because of the important weight increase caused by the required water storage.

In addition to the above-mentioned actuators, fluidic control has also been investigated using pulsed microjets. When dealing with fluid injection, a major interest of such a control is the reduction of the injected mass flow rate. Ragaller (Ragaller et al., 2009) for instance demonstrated the capacity of achieving with a reduced mass flow pulsed control a noise decrease close to that obtained with continuous water injection.

Noise reduction through energy injection using plasma actuators is also being investigated for subsonic (Kastner et al., 2008; Kearney-Fischer et al., 2009a;b; Kim et al., 2009; Samimy et al., 2007a) and supersonic (Kearney-Fischer et al., 2011; Samimy et al., 2007b) jets. Control is made with localized arc filament plasma actuators, each actuator consisting in a pair of pin electrodes and generating electric discharge plasmas at a driven frequency varying from 0 to 200 kHz. Authors especially observed a broadband noise increase for low forcing frequency excitation, below $St_F = 1$, and a reduction for higher frequencies. This noise reduction is especially improved with increasing main jet temperature.

Only a limited number of numerical works have been published on the action of continuous air microjets for noise reduction (Enomoto et al., 2011; Laurendeau et al., 2008; Najafi-Yazdi et al., 2011; Rife & Page, 2011; Shur et al., 2011). Except for the simulation of Lew (Lew et al., 2010), they all modelled the microjets to avoid gridding the feed pipes. Those simulations illustrate the capacity of Large Eddy Simulations (LES) to capture the effect of microjets on both flow and noise, even using modelled actuators. To the knowledge of the authors, no simulations have been published on the action of pulsed actuators for jet noise control.

In the present work, a circular jet with an acoustic Mach number $M_a = U_j/c_0 = 0.9$ (U_j being the axial jet exhaust velocity and c_0 the ambient sound speed) is computed by LES. Simulations are performed for two main jet temperatures, corresponding to isothermal ($T_j = 288K$) and heated ($T_j = 576K$) flows with a Reynolds number based on nozzle diameter D of $Re_D = U_j D/\nu = 1,000,000$ and 320,000 respectively, where ν stands for the kinematic viscosity.

The choice of those configurations is justified by the presence of aerodynamic and acoustic measurements previously performed without control by Institut PPRIME in Poitiers, France, during the JEAN European project, as well as aerodynamic and acoustic measurements realised by Castelain for the same nozzle and isothermal jet condition, with similar microjets configurations (Castelain et al., 2007; 2008). To complete those data, a new set of acoustic measurements has been conducted by Institut PPRIME during the project, to provide far field pressure data for the baseline and continuous microjets simulated configurations.

The paper is organised as follows. The test cases used for the simulations are recalled in section 2, with details given on the methodology used for both aerodynamic and acoustic simulations. Special focus is made on the modelling of the microjets. Section 3 corresponds to a detailed analysis of the aerodynamic fields. Mean and r.m.s. velocity profiles are presented and flow modifications with control are discussed. This part ends with a linear jet stability

analysis. Acoustic results are then reproduced in section 4. Comparisons between simulations and experiments are made when available and changes in spectra shapes and integrated levels are analyzed. Relations are made with the evolutions previously noticed in the flow. Paper finally ends with concluding remarks and perspectives in section 5.

2. Simulation parameters

Aeroacoustics simulations are performed in two separate steps. Instantaneous flow simulations are conducted in a first time to compute the noise sources in the jet. To provide the best possible flow resolution with existing computed resources, accurate Navier-Stokes simulations are restricted to the jet plume, during which instantaneous aerodynamic fields are stored on surfaces surrounding the jet. Those fields are then used as source data for noise radiation to the microphones, using a surface integral method.

2.1 Aerodynamic numerical specifications

Aerodynamic simulations are performed using the flow solver CEDRE developed at Onera. CEDRE is a multi-physics, reactive solver used by researchers and aeronautical industries for engine conception and optimisation, such as combustion (Dorey et al., 2010; Dupoirieux & Bertier, 2011), turbine blade cooling (Guillou & Chedevergne, 2011) and jet noise (Bodard et al., 2009), for instance. Navier-Stokes equations are solved using second order upwind schemes space discretization for generalised polyhedral computational grids (Courbet et al., 2011) with explicit or implicit time schemes from first to third order for time resolution.

In the present simulations, the fluctuating jet flow is solved using the LES model with the MILES approach (Boris et al., 1992; Fureby & Grinstein, 1999; Grinstein & Fureby, 2002), where the dissipation of the structures smaller than the grid size is not modelled and is assumed to be of the order of the numerical dissipation. The validity of this approach for jet simulations relies on the hypothesis proposed by Biancherin (Biancherin, 2003) that those unresolved scales do not notably influence the noise generation in the flow. This assumption has been verified by Muller (Muller et al., 2006), who compared jet flow and noise results obtained using either the Smagorinsky subgrid scale model (Smagorinsky, 1963) or the MILES approach and observed very similar results.

The current approach developed for jet noise simulations is based on the inclusion of the nozzle geometry in the computational domain, which provides many advantages compared to simulations limited to flow domain only.

The first advantage is the absence of artificial disturbance at nozzle exit to destabilize the flow. Freund (Freund, 2001) and Bogey (Bogey et al., 2003), for instance, illustrated the necessity to add numerical perturbations over the imposed mean flow profile for the jet to be destabilized and to generate turbulence, with the risk of generating spurious noise. With the present approach, it is expected that by removing boundary conditions from a critical location, where instability waves must be allowed to develop freely, one permits some kind of natural growth of instability waves to occur. Indeed, Biancherin (Biancherin, 2003) and Muller (Muller, 2006) highlighted that, with this procedure, small truncation errors destabilize the flow and no more artificial excitation is needed at nozzle exit.

The inclusion of the nozzle all the more permits the simulation of complex, realistic geometries such as short-cowl nozzles with the inclusion of a pylon, bifurcations and chevrons (Eschricht

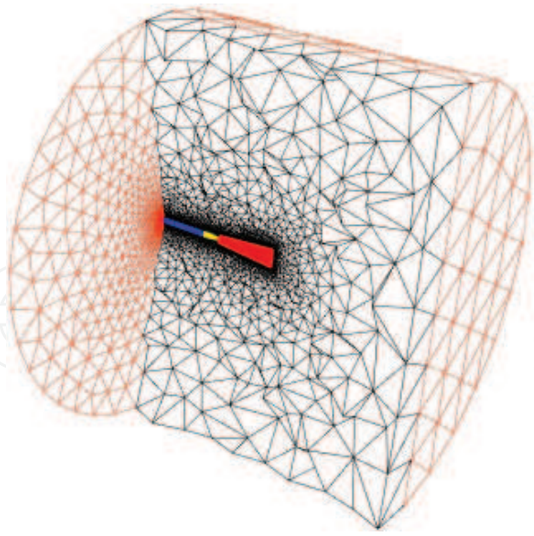

Fig. 1. Illustration of half the computational domain. Orange elements correspond to external boundaries, yellow to nozzle surfaces, blue to upstream fairing, red to structured patch and black to unstructured elements.

et al., 2008; Uzun & Hussaini, 2009; Xia et al., 2008; Yan et al., 2007). The increased difficulty in mesh generation is overtaken in the present case by the use of an unstructured grid generator.

The full numerical domain is a cylinder with length and radius of 120 D and 84 D respectively, mainly composed of tetrahedrons. Those important dimensions, far greater than the requested noise source generation domain, give possible the use of large sponge zones to avoid spurious noise reflections at the outlet boundaries of the computational domain, where static pressure is imposed. Inlet boundaries correspond to imposed total pressure and temperature at nozzle inlet and imposed velocity and static temperature at external flow inlet.

According to Zaman (Zaman, 1985), nozzle exit boundary-layer momentum thickness of a high Reynolds number jet of about 10^6 is $\delta_\theta/D \sim 10^{-3}$. Proper numerical resolution of such a thin boundary layer is unreachable with present computational power. The objective of the study being to illustrate the capacity of the simulations to quantitatively reproduce the noise reduction effect of microjets for industrial interests, it is chosen to restrict the grid size to affordable simulations with preferred high resolution of the flow in noise production regions. Boundary layers are thus under-resolved in the present computations, with the momentum thickness being roughly $\delta_\theta/D \sim 0.2$. This value is for instance four times larger than the one already used for other simulations of Mach 0.9 jets (Bodony & Lele, 2005; Bogey et al., 2003).

To increase resolution of the turbulence in the jet plume, a structured patch represented in red on Fig. 1 is included in the computational grid behind the nozzle exit. This truncated cone extends axially from $x/D = 0$ to $x/D = 25$, and radially to $r/D = 2$ and 4, respectively, at the two previous axial positions. Its construction is based on a 2D grid, rotated around the jet axis to provide 60 azimuthal hexahedral elements. The central part of the mesh is modified with a O-grid configuration illustrated on Fig. 2 to ensure homogeneous sized cells in the jet core.

The construction of the structured patch is based on aerodynamic and acoustic criteria to ensure sufficient resolution of flow development and sound propagation. First criterion ensures a sufficient resolution of the sheared flow and relies on the estimation of the jet

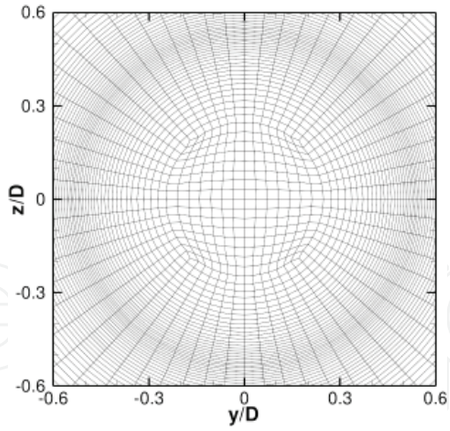

Fig. 2. Detail of the O-grid configuration used on jet axis. Axial position $x/D = 1$.

shear layer thickness δ by Candel and already used in previous simulations (Biancherin, 2003; Muller, 2006):

$$\frac{\delta}{D} = 0.153\left(\frac{x}{D}\right) + 0.002 \tag{1}$$

Outside of the flow development region, an acoustic criterion is chosen to properly propagate acoustic waves to the storage surfaces used for noise radiation (see §2.3). For subsonic jets, where noise comes from flow mixing, dominant pressure waves are observed for Strouhal numbers $St = fD/U_j$ below 0.3. It is thus chosen to radiate noise with negligible dissipation up to $St = 0.5$, which provides most of the energy contained in the pressure spectra. Biancherin (Biancherin, 2003) demonstrated that, with the numerical methods used in the flow solver, a minimum of 20 points per wavelength is required for a correct propagation of the pressures waves over the distances considered with the constructed numerical grid.

In the present case, radial resolution is set to resolve the shear layer with 20 cells at an axial distance of 1 D after the nozzle exit, where the radial size of the cells is chosen to double between centreline and exterior of the shear with a regular growth of 7%. The same radial growth rate is used outside of the shear layer up to the end of the structured patch and satisfies the acoustic criterion for correct noise resolution. A 9.5% growth rate is used between the shear layer and the jet axis, where larger turbulent structures are expected to be observed especially after the end of the potential core.

Axial size of the elements is imposed at nozzle exit and is similar to the radial extent of the elements used in the shear layer at jet exhaust. Axial stretching of 1% is used until the elements reach the maximum size given by the acoustical criterion, after what no growth rate is applied.

The structured patch is composed of 1.6×10^6 hexahedra, for a total mesh of 4.5×10^6 cells. An illustration of the mesh at nozzle exit is given on Fig. 3 (a).

Construction of such grids leads to a limited amount of very small elements close to the nozzle exit, where velocity and temperature reach their maximum values. The use of an explicit time scheme would thus oblige one to run simulations with a very low time step verifying the CFL condition $(u + c)\,\Delta t/\Delta x < 1$, which can be very penalizing for efficient and quick simulations. Proper flow resolution in those elements not being critical for an accurate description of the whole jet, time resolution is performed with a first order implicit time scheme that allows CFL criterion above 1 in those cells, and thus an acceptable time step. Use of such a scheme is not a problem for noise propagation: results from previous

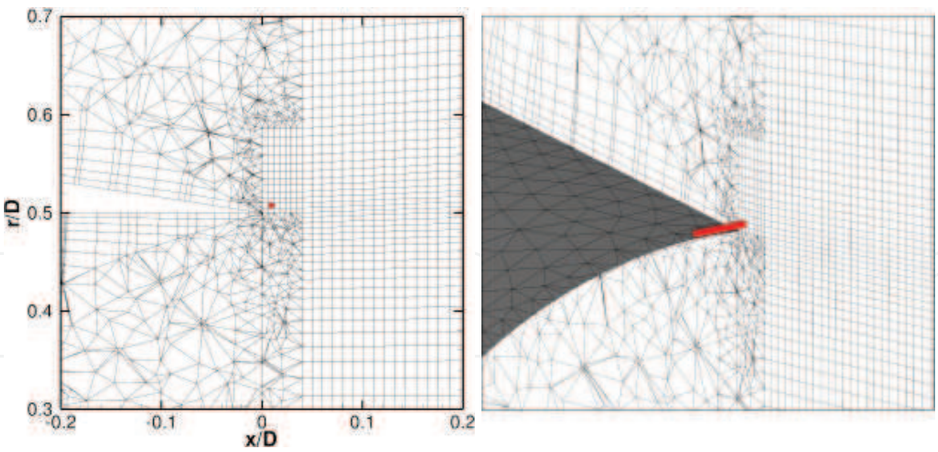

(a) detail of nozzle exit and mesh adaptation to model the microjets

(b) 3D illustration of the cell used for microjet injection (in red)

Fig. 3. Mesh adaptation for microjets modelling. Planar cut of volume mesh is represented in black, nozzle in grey and microjet cell in red.

studies demonstrated that, thanks to the very small time step in the acoustic propagation area (chosen to verify a CFL condition lower than 1 in the flow), the first order implicit time scheme is sufficient for a correct wave propagation and is consequently used in the present study.

2.2 Microjets modelling

To avoid the necessity of very small sized cells and restricting time step for the microjets representation, a simplified model corresponding to volume sources located in specific cells is employed. The objective of this approach is not to provide an extremely precise and detailed description of the actuators. It is used to investigate the concept of flow injection for noise reduction, which is numerically challenging and even innovative for pulsed actuators. One must furthermore keep in mind that this approach should in the future be used for larger scale, double stream configurations, for which a detailed description of the microjets will not be numerically affordable in the near future due to the complexity of the configurations.

To reproduce the geometric configuration used experimentally, where the microjets are located very close to the nozzle lip, the structured patch has been extended near the jet exit, as illustrated on Fig. 3.

With the present approach, the mass injection and convection due to the microjets is modelled through source terms in the equations of mass ($\dot{m}$), momentum ($\dot{m}\vec{U}$) and energy ($\dot{m}E$) in specific hexahedral cells, identified as the locations of the microjets.

The choice is made here to calibrate the microjets with their velocity and temperature. Velocity vector $\vec{U}$ corresponds to the orientation and velocity of the injected fluid and energy E is given by the following formula:

$$E = h_{ref} + Cp\left(T - T_{ref}\right) + U^2/2 \tag{2}$$

where T_{ref} is the reference temperature, h_{ref} the enthalpy of formation at reference temperature and Cp the calorific capacity at constant pressure.

To ensure that the computed velocity and temperature correspond to the desired values, the mass flow rate $\dot{m}$ is determined through an iterative process. Based on the aimed velocity and temperature, an estimation of the initial mass flow rate can be calculated using the fluid velocity, its density and the surface S used for the injection: $\dot{m} = \rho U S$, where density is approximated by considering that the microjet flow occurs at ambient pressure. The surface can be evaluated from cell geometry and velocity vector: $S = \vec{U} \cdot \vec{S}/U$ with $\vec{S} = \sum_i S_i \cdot \vec{n}_i$ the sum of downstream exhaust surfaces S_i of the hexahedral cell used for microjet injection and $\vec{n}_i$ their associated outside-oriented normal vectors.

Using this iterative approach, mass flow rate is updated at each iteration until velocity and temperature reach the target values. From the computed surface used for the injection, it is in addition possible to evaluate the equivalent microjet diameter, considering a circular microjet nozzle : $d_{eq} = 2\sqrt{S/\pi}$.

2.3 Noise radiation

Instantaneous flow fields provided by the flow simulation and stored on surfaces are used to radiate sound to the microphones. Several integral formulations such as Lighthill (Lighthill, 1952), Kirchhoff (Lyrintzis, 1994) and Ffowcs Williams & Hawkings (FW-H) (Ffowcs Williams & Hawkings, 1969) are available to reconstruct far field noise from volume or surface fluctuations. It is usually preferred to use surface fields to limit the amount of stored data and numerical operations required to perform the noise radiation, which is done in the present study. Lighthill volume integral formulation can nevertheless be fruitful if one wants to identify the noise sources present in the flow (in Lighthill's sense), as done by Perez (Perez et al., 2007).

Based on the extended investigations performed on the topic by Rahier (Rahier et al., 2004), noise radiation is performed in the present case using FW-H porous surface formulation. In their paper, the authors especially demonstrated that this formulation makes it possible to place the control surface rather close to the jet, in a non-uniform flow. The surface position requirement is that the non-uniformities of the flow on the control surface are only due to convected gradients (such as density gradients related to thermal mixing in the case of a hot jet) and are not high sources of noise production (such as instability expanding or vortex pairing). On the contrary, the Kirchhoff method (with density or pressure as input data) is a much less suited tool for acoustic post-processing of jet aerodynamic simulations because of its high sensibility to non acoustic density or pressure gradients (local thermal mixing or vorticity).

Control surfaces are moreover kept open at both extremities. Investigations indeed showed that closing the surface leads in the best case to results similar as with open surface and can provide erroneous results if the control surface is too short, because of the turbulence level on the downstream closing disc. As a consequence of using an open control surface, its axial extent needs to be sufficiently large for a correct radiation at low angles, where the maximum noise is expected. It practically leads to a length of 20 to 25 nozzle diameters.

An axial extent of 25 diameters is used for the present simulations. Surfaces additionally verify $1 \leq r/D \leq 2$ at nozzle exit and $3 \leq r/D \leq 4$ at the downstream end. Radiation is performed for 4 different surfaces. Collapsing time signals and pressure spectra in the far field ensure that the surfaces enclose all noise sources and provide a limited dissipation for frequencies below a Strouhal number of 0.5.

T_s (K)	U_j (m/s)	M_a	M_j	Re_D	Q_j (kg/s)
288	306.65	0.90	0.90	1.0×10^6	0.723
576	306.65	0.90	0.64	3.2×10^5	0.362

Table 1. Main jets experimental characteristics.

To end, computed spectra and integrated pressure levels are azimuthally averaged over 48 microphones located around the jet axis. In the present case of an axisymmetric geometry, far field noise is indeed expected to be statistically independent of the azimuth, which is not the case for short-time duration computed signals and can lead to differences of almost 2 dB (Huet et al., 2009).

2.4 Simulated configurations and numerical procedure

The nozzle used for the simulations is a convergent single stream nozzle with an exhaust diameter $D = 50$ mm. Two main jet configurations, corresponding to isothermal and heated flow, are investigated, which main characteristics are recalled on Table 1. Those configurations correspond to the baseline and are used as reference when investigating the effect of microjets on flow and noise.

Based on grid construction and flow characteristics, the aerodynamic time step is set to $\Delta t_{aero} = 10^{-6}$ s, which corresponds to a CFL criterion lower than 1 in most of the computational domain. Surface storage is performed every 10 iterations of the flow simulation, $\Delta t_{acou} = 10^{-5}$ s. It corresponds to a maximum frequency of 50 kHz, which ensures that every frequency correctly resolved by the LES will be properly radiated using the integral formulation.

The control of the jet is performed with the use of 12 microjets regularly positioned around the nozzle lip, just after the exhaust area, with an impinging angle of 45 degrees relative to the jet axis. Continuous microjets are computed for both main jets. Pulsed microjets, for which simulations are run as exploratory computations only, are just performed for the isothermal configuration with all actuators in phase, which corresponds to the axisymmetric mode $m = 0$. Their flow and geometrical characteristics are identical to those used for the continuous microjets; time modulation of the source terms is a periodized crenel, whose value is set to 1 during $1/3^{\text{rd}}$ of the period and 0 otherwise. This modulation is a first representation of the plasma synthetic jets developed at Onera for flow and noise control (Caruana et al., 2009; Hardy et al., 2010). The two forcing frequencies $f_F = 3$ kHz and 9 kHz are considered for the simulations. They are chosen following the experimental results of Samimy (Samimy et al., 2007a) using localized arc filament plasma actuators and who observed a broadband noise increase for the low frequency excitation and a reduction for the high one.

For all simulations, microjets velocity and temperature are set to 300 m/s and 288 K respectively. Those values correspond to the ones used for the main isothermal jet.

Equivalent microjet diameter is $d_{eq} = 1.27$ mm. This diameter is comparable to the 1 mm diameter of the actuators used at Institut PPRIME during the acoustic test campaign of the project and by Castelain (Castelain et al., 2007; 2008) for aerodynamic and acoustic measurements performed in a separate framework. The distance between the microjets and the main jet shear layer is $0.40\, d_{eq}$. It ensures that the microjets flow spreading is very limited before reaching the jet flow and that its action on the shear layer is not negligible.

	x_c/D	$u'_{x\,rms}/U_j$ max at $r/D=0$	$u'_{x\,rms}/U_j$ max at $r/D=0.5$ $(x/D>1)$
isothermal jet, baseline experiment	7.9	0.135	
heated jet, baseline experiment	6.3	0.155	
isothermal jet, baseline	5.2	0.167	0.186
isothermal jet, continuous microjets	5.7	0.159	0.183
isothermal jet, $f_F = 3$ kHz pulsed microjets	7.1	0.178	0.211
isothermal jet, $f_F = 9$ kHz pulsed microjets	6.6	0.153	0.176
heated jet, baseline	4.1	0.168	0.195
heated jet, continuous microjets	4.7	0.187	0.198

Table 2. Axial position of the end of the potential core x_c and peak axial r.m.s. velocity along the jet axis and the shear shear.

The computed injected mass for each continuous microjet is $Q_{mjet} = 4.8 \times 10^{-4}$ kg/s. This value is 5% more important than the estimation made at the beginning of the iterative process, based on fluid velocity, estimated density at ambient pressure and injection surface: $Q_{th} = 4.6 \times 10^{-4}$ kg/s. The small difference can come from pressure variations at microjets injection. The mass flow rate ratio per microjet $r_m = Q_{mjet}/Q_j$ is $r_m = 6.7 \times 10^{-4}$ for the cold jet and $r_m = 1.3 \times 10^{-3}$ for the heated one.

Microphones are located 50 diameters from the nozzle exit. JEAN experimental results, performed at a distance of 30 D, are rescaled to 50 D using the far field acoustic approximation with $1/r$ pressure amplitude decrease. Integrated pressure levels are computed for frequencies between 300 Hz and 41 kHz. The upper limit is higher than the grid cut-off frequency given in §2.1 because one of the objectives of the approach developed at Onera and used here is to compare simulations to experiments on the experimental frequency bandwidth. The underestimation of the computed OASPL caused by the poorly resolved high frequency levels is nevertheless negligible because the major part of the energy is contained in the low frequency range, below $St = 0.5$, that is accurately resolved in the simulations.

The numerical procedure used for all simulations is the following. Every aerodynamic simulation starts from rest and inlet pressure is progressively increased to reach the target value. Computation is then run until the flow is developed in the refined domain, after what surface storage and mean flow averaging begins. The storage is performed during 50 ms of simulated time, which corresponds to 300 D/U_j convective time units. This duration ensure statistically converged mean flow fields and sufficiently resolved far field pressure spectra in the frequency domain for further analyses.

3. Aerodynamic results

3.1 Reference simulations

Evolution of mean axial velocity and turbulent axial velocity along the jet axis are represented on Fig. 4 for the reference simulations. For both temperatures the potential core length, defined as the axial distance from the nozzle exit at which $U_x/U_j = 0.9$ and reported on Table 2 is about 30% shorter in the simulation compared to the experiment. Both simulations moreover overestimate the peak axial r.m.s. velocity on the jet axis.

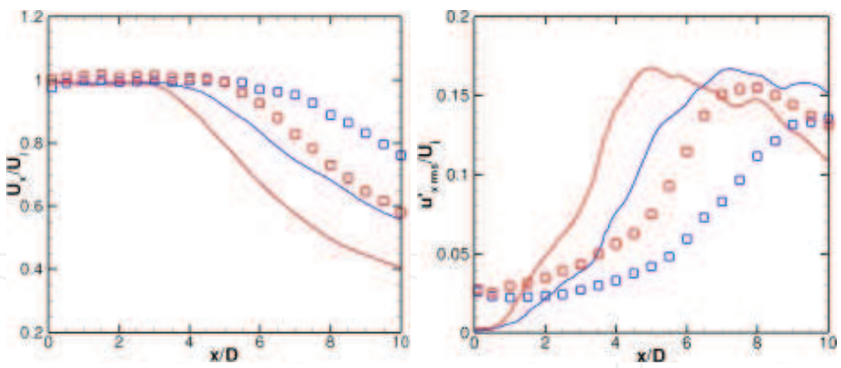

(a) axial mean velocity (b) axial r.m.s. velocity

Fig. 4. Experimental and simulated axial (a) mean and (b) r.m.s. velocity on jet axis for isothermal (blue) and heated (red) baseline configurations. □ experiments; – simulations.

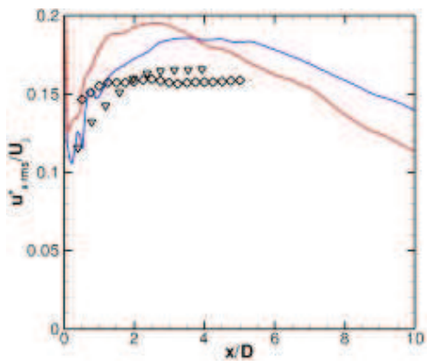

Fig. 5. Evolution of the axial r.m.s. velocity u'_{rms} along the nozzle lip. Simulations: – isothermal and – heated baseline configurations. Measurements: ◊ Husain and Hussain for an initially turbulent shear layer (Husain & Hussain, 1979) and ∇ Fleury et al. for a Mach 0.9 jet at $Re_D = 7.7 \times 10^5$ (Fleury et al., 2008).

This numerical underestimation of the potential core length has already been observed in previous computations of the same geometry (Andersson et al., 2005; Bodard et al., 2009; Bogey & Bailly, 2006) and might come partly, in the present computations, from different initial conditions between experiments and simulations. Fig. 4 (b) illustrates the differences between experimental and simulated turbulence levels at nozzle exit, experiments exhibiting the presence of velocity perturbations which are not present in the computations. These very low computed turbulence levels are a consequence of the unperturbed inflow imposed on the nozzle inlet boundary and may be the reason of the discrepancies observed. Bogey (Bogey & Bailly, 2010) indeed numerically demonstrated for a $M_j = 0.9$ and $Re_D = 10^5$ jet that the presence of disturbances in the nozzle increase the potential core length and lower the turbulence levels on the jet axis.

Simulated turbulence profiles along the nozzle lip reproduced on Fig. 5 exhibit a peak value for $x/D \sim 4$ and $x/D \sim 3$ respectively for the isothermal and the heated jet, whereas those turbulence levels increase nearly monotonically for experimental fully turbulent jets also reported on the figure. These peak r.m.s. values might indicate a strong transition of the initially laminar jet mixing layer in the computations.

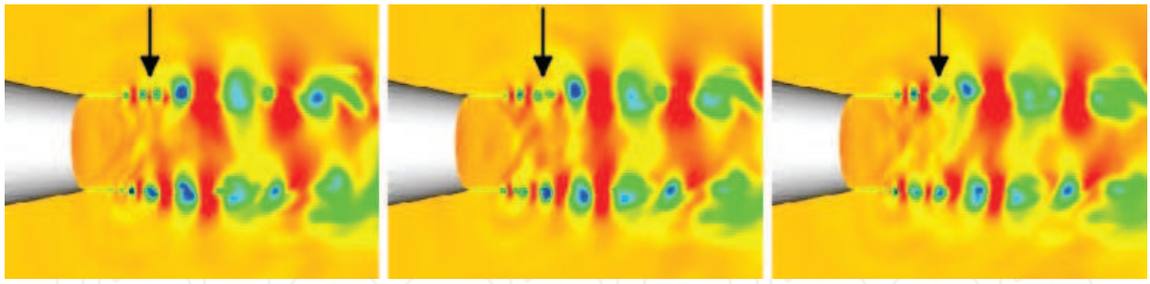

Fig. 6. Illustration of the vortex pairing phenomenon (arrow) observed for the isothermal simulated jet. Coloured map represents density field at 3 different instants.

With the considered Reynolds numbers, the shear layer is expected to be fully turbulent for the isothermal jet or at least nominally turbulent for the heated jet, using the terminology proposed by Zaman (Zaman, 1985). Its initially laminar state might be explained by the unperturbed imposed inflow as well as the lack of resolution of the boundary layers of the nozzle. This low discretization would not allow sufficient resolution of the perturbations that are expected to develop and to trigger the turbulent shear layer development. Similar observations have been made by Vuillot (Vuillot et al., 2011) on a double stream nozzle with external flow.

An illustration of the initially laminar shear layer development is visible on Fig. 6 for the isothermal jet. One can first observe on the instantaneous density field represented at three different instants a vortex shedding phenomenon, corresponding to the green dots along the shear layer. This shedding is followed by multiple vortex pairings occurring 1 diameter or more after the nozzle exit, one of them being visible in the pictures at the end of the arrow. These phenomena are characteristic of laminar to turbulent transition in the mixing layer, explaining the peak axial r.m.s. velocity observed on Fig. 5 for the computations.

In addition to the initially laminar state of the computed jets, the overestimation of the turbulence observed on Fig. 4 (b) and on Fig. 5 might also come partly from a too fast coarsening of the grid in the axial direction. Indeed, a coarse grid tends to overestimate the large turbulent structures and thus the turbulent kinetic energy, leading to a too fast growth of the shear layers and a shortening of the potential core.

Despite those discrepancies between the simulations and the experiments, the effect of temperature on mean and r.m.s. velocities is well reproduced by the simulations, with a reduction of the potential core length of 20% with increasing temperature for both measurements and computations. The consequence of this core length shortening is the reduction of the axial distance at which the peak axial r.m.s. velocity occurs. The peak axial r.m.s. level increase observed experimentally on the jet axis with increasing temperature is nevertheless not clearly visible in the simulations, with only a 0.5% raise compared to 20% in the experiments. Higher turbulence levels for the heated jet are however observed numerically along the shear layer.

3.2 Continuous microjets

No aerodynamic measurements being available for the simulated configurations with microjets, investigations presented hereafter are performed comparing baseline and controlled simulation with available literature results.

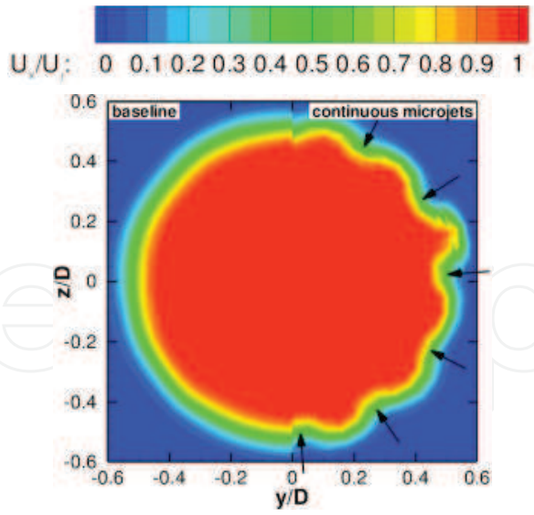

Fig. 7. Mean axial velocity computed at $x/D = 1$ for the baseline (left) and continuous microjets (right) isothermal configurations. Arrows represent the position of the microjets.

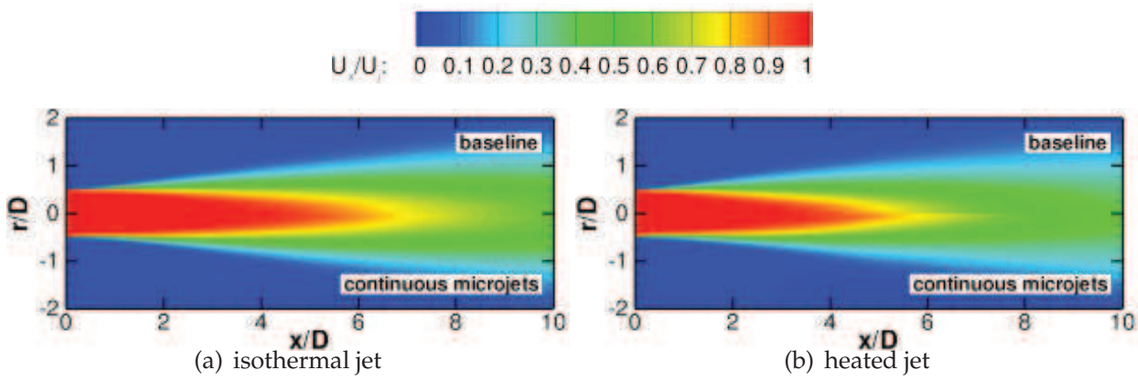

(a) isothermal jet (b) heated jet

Fig. 8. Mean axial velocity distribution for (top) baseline and (bottom) continuous microjets configurations. Plane located through microjet position.

An illustration of the efficiency of the microjets for modifying main jet mean flow is visible on Fig. 7. It is clearly visible on this figure that the actuators corrugate the jet azimuthally by locally decreasing the axial velocity downstream of the microjets. These corrugations are limited in space to the nozzle vicinity and vanish more downstream after 3 diameters, as experimentally observed (Alkislar et al., 2007; Arakeri et al., 2003; Castelain et al., 2007). They are a consequence of the difference in axial velocity between the microjets and the main jet that is expected to generate flow mixing.

Cartographies of mean axial velocity, reproduced on Fig. 8, illustrate a stretching of the jet with the presence of the microjets. This stretching is accompanied by an increase of the potential core length of 10% and 15%, respectively for the isothermal and heated configurations, especially visible on Fig. 12 (a). This result is consistent with the experimental observations of Castelain et al. and Arakeri et al., the latter observing an increase of 25% caused by the control.

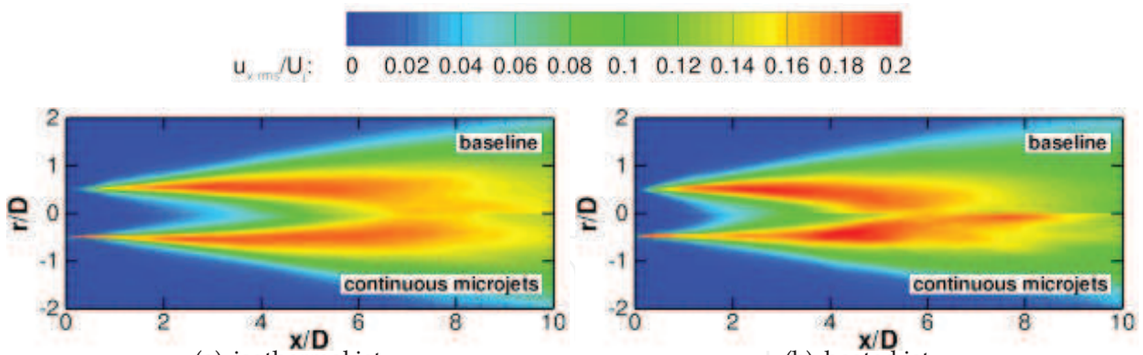

(a) isothermal jet (b) heated jet

Fig. 9. Axial r.m.s. velocity distribution for (top) baseline and (bottom) continuous microjets configurations. Plane located through microjet position.

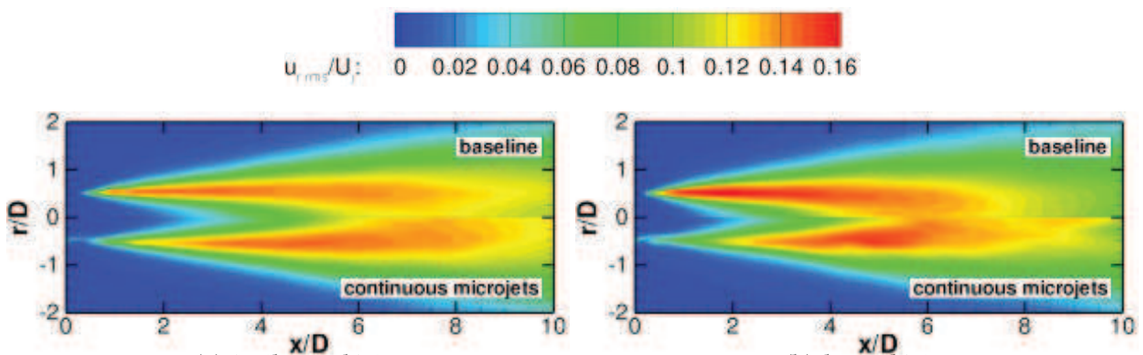

(a) isothermal jet (b) heated jet

Fig. 10. Radial r.m.s. velocity distribution for (top) baseline and (bottom) continuous microjets configurations. Plane located through microjet position.

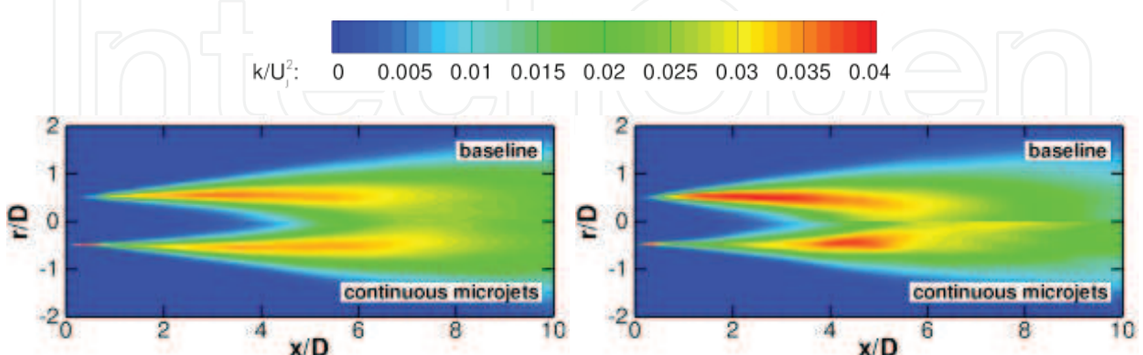

(a) isothermal jet (b) heated jet

Fig. 11. Turbulent kinetic energy distribution for (top) baseline and (bottom) continuous microjets configurations. Plane located through microjet position.

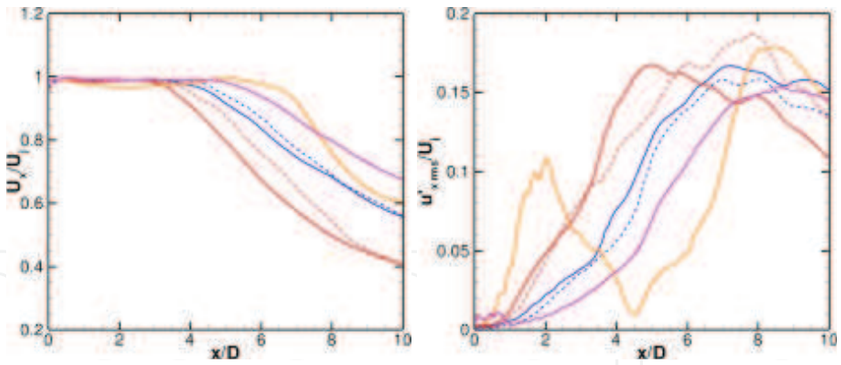

(a) axial mean velocity (b) axial r.m.s. velocity

Fig. 12. Simulated axial (a) mean and (b) r.m.s. velocity on jet axis. Isothermal jets: – baseline; – – continuous microjets; – $f_F = 3$ kHz pulsed microjets; – $f_F = 9$ kHz pulsed microjets. Heated jets: – baseline; – – continuous microjets.

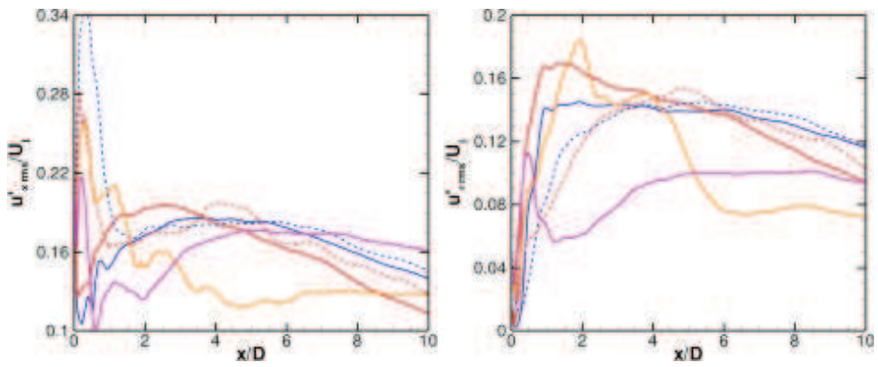

(a) axial r.m.s. velocity (b) radial r.m.s. velocity

Fig. 13. Evolution of the r.m.s. velocities along the nozzle lip. The legend is the same as on Fig. 12.

As experimentally expected, the presence of the microjets also leads to a reduction of the peak axial r.m.s. velocity on the jet axis for the isothermal jet, see Fig. 12 (b). This peak value is however increased for the heated jet and is a consequence of a spot of high axial velocity fluctuations appearing near the jet axis for $x/D = 8$, as visible on Fig. 9. Except for this spot, no significant modification of the peak value is observed for the heated jet, its axial location being shifted downstream compared to the baseline configuration because of the more important jet stretching relative to the isothermal simulations.

Along the shear layer and for the isothermal jet, actuators lead to a reduction of the turbulence in the first diameters after the nozzle exit, see Fig. 13. This result is similar with the observations of Castelain (Castelain, 2006). It nevertheless slightly differs from the results of Arakeri (Arakeri et al., 2003) who measured a reduction of the peak axial r.m.s. velocity that is not reproduced by the simulations. Similar flow modifications are observed for the heated jet, except for the peak radial r.m.s. velocity that is now reduced in the computations.

Such modifications in the turbulent velocities numerically lead, for both temperatures, to a reduction of the peak turbulent kinetic energy in the jet plume, that appears further

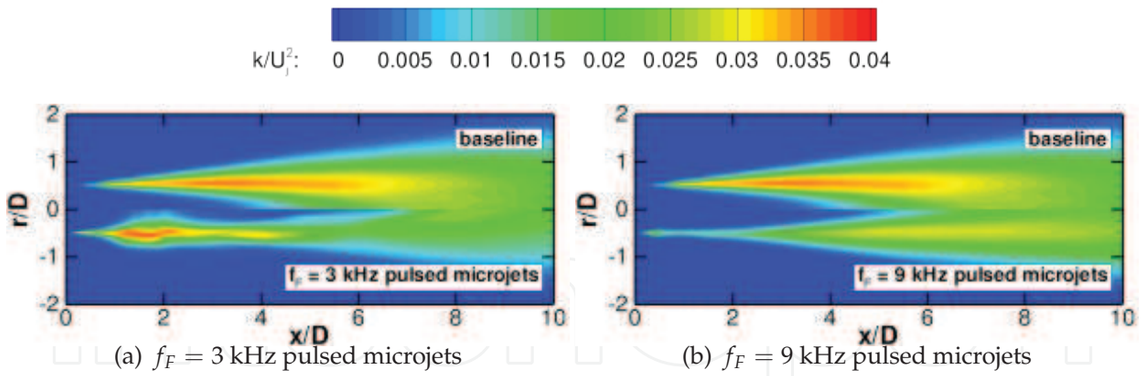

(a) $f_F = 3$ kHz pulsed microjets (b) $f_F = 9$ kHz pulsed microjets

Fig. 14. Turbulent kinetic energy distribution for (top) baseline and (bottom) pulsed microjets configurations. Plane located through microjet position.

downstream from the nozzle exit compared to the baseline configurations, as visible on Fig. 11. On this figure is also observed a high turbulence level just downstream of the microjets injection, that comes essentially from the contribution of the axial turbulent velocity. This increase is not observed in the experiments and can be attributed in the present simulations to the initially laminar shear layer.

3.3 Pulsed microjets

Despite the initial state of the shear layer that is not fully turbulent in the simulations, which leads especially to some differences on flow characteristics with the experiments, all the aerodynamic simulated results with continuous microjets presented in the section above compare rather well with the experimental data. This tends to illustrate that the actions of the actuators on the main jet are correctly reproduced in the computations. A further investigation on the efficiency of such a type of control is thus performed by considering pulsed microjets. It has to be recalled nevertheless that the modelled pulsed actuators do not intend to precisely reproduce the existing plasma synthetic jets developed at Onera (Caruana et al., 2009; Hardy et al., 2010), but are used to illustrate the capacity of the numerical code to reproduce the action of such microjets.

Fig. 12 illustrates the more important potential core length increase obtained with the pulsed control, compared to the continuous one. This core increase is related for both simulations to the reduction of the axial r.m.s. velocity along the shear layer, the more important reduction being observed for the high frequency excitation. This turbulence reduction observed for the $f_F = 9$ kHz forcing is qualitatively similar to the one occurring with continuous microjets, for both axial and radial turbulent velocities, and is simply more pronounced, as visible on Fig. 13. This is clearly visible when looking at the turbulent kinetic energy distribution, reproduced on Fig. 14 (b).

A different evolution of the turbulence is observed for the low frequency forced jet. Velocity fluctuations present in this case a very large increase a few diameters after the nozzle exit, the peak turbulent kinetic energy being localized about 1.5 D downstream of the jet exit, see Fig. 14 (a). The oscillations observed on this figure only come from the too short time duration in the averaging and are caused by the strong response of the jet to the excitation, visible on Fig. 15 (c), and which was not observed with continuous or $f_F = 9$ kHz pulsed control.

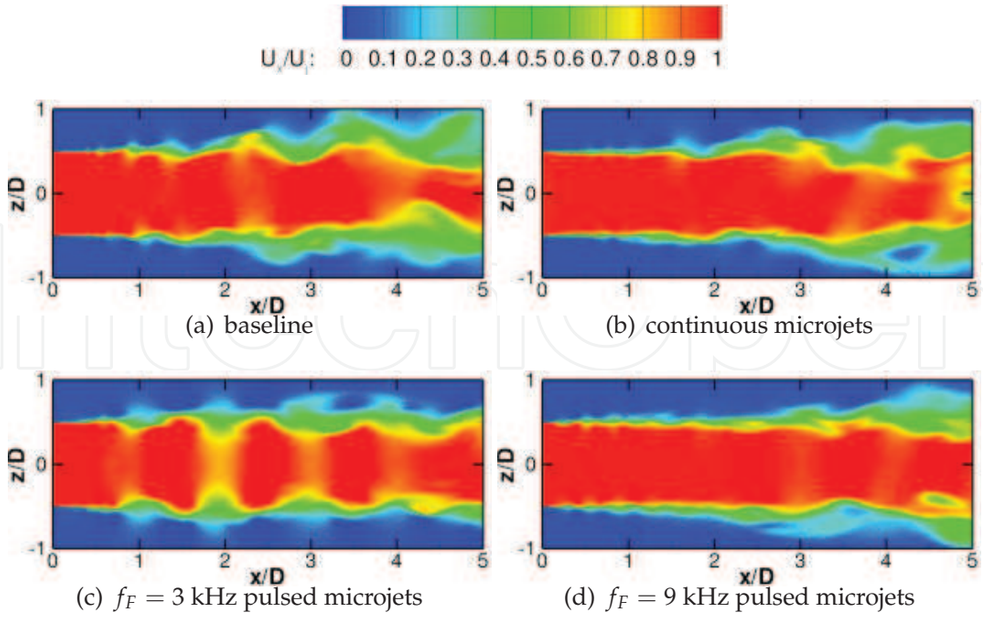

(a) baseline (b) continuous microjets

(c) $f_F = 3$ kHz pulsed microjets (d) $f_F = 9$ kHz pulsed microjets

Fig. 15. Instantaneous axial velocity distribution on $y = 0$ plane. Isothermal jet simulations.

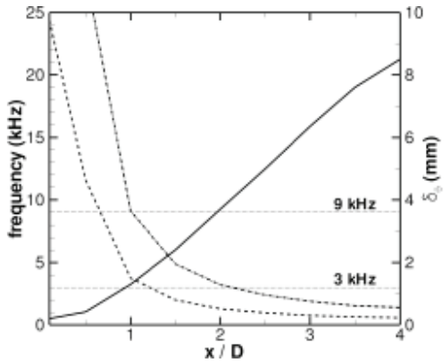

Fig. 16. Evolution of the (–) momentum thickness, (– –) most unstable shear layer frequency and (– ·) neutral disturbance frequency. Baseline isothermal jet simulation.

To explain this distinct response of the flow to the $f_F = 3$ kHz pulsed excitation, a jet stability analysis is performed on the baseline configuration, using Michalke's theoretical work on the stability of inviscid shear layers (Michalke, 1965). In this theory, the radial profile of the axial velocity is analytically represented with an hyperbolic-tangent profile:

$$U(r) = \frac{U_j}{2}\left(1 + tanh\left(\frac{r}{2\delta_\theta}\right)\right) \tag{3}$$

where r represents the radial distance from the axis and δ_θ the momentum thickness. The most unstable shear layer frequency is then given by $f = 0.0165 \cdot U_j/\delta_\theta$ and the neutral disturbance frequency by $f = 0.0400 \cdot U_j/\delta_\theta$. This last frequency corresponds to the threshold value for which the excited shear layer modes are stable and thus do not lead to a destabilization of the jet.

In the present simulation, the hyperbolic-tangent velocity profiles well fit the simulated profiles in the first jet diameters. More downstream some differences can be observed between simulated and analytical profiles, that might lead to an underestimation of the calculated frequencies. The modelling however gives a correct order of those two characteristic frequencies of the shear layer.

The evolution of the momentum thickness in the first diameters after the nozzle exit is represented on Fig. 16. On this figure are also visible the most unstable shear layer frequency and the neutral disturbance frequency. It is clearly observed that both frequencies of 3 kHz and 9 kHz correspond to most unstable frequencies within the first diameter after the nozzle exit. However, the neutral frequency is observed just downstream for the 9 kHz frequency, which can explain that no destabilization is noticed: each instability appearing in the jet is nearly instantaneously damped. This damping is theoretically expected further in the jet for 3 kHz perturbations, which gives the time for the shear layer instabilities to develop. This result is coherent with the illustration of the instantaneous axial velocity on Fig. 15 (c), where strong oscillations are observed with the $f_F = 3$ kHz pulsed control for $x/D = 1$.

4. Acoustic results

Noise modifications caused by temperature increase and microjets are presented in this section. Simulations with continuous control are compared to measurements provided in the frame of the study by French institute PPRIME for angles above 50 degrees. Experimental data from European project JEAN, also performed by institute PPRIME, are nevertheless preferred for temperature effect investigation, as they provide noise levels below 50 degrees. Comparisons have been made to ensure that both experimental campaigns provide similar results.

4.1 Temperature effect

The effect of temperature on jet noise has been widely investigated experimentally (Tanna, 1977; Tanna et al., 1975; Viswanathan, 2004). It has been observed that, for a fixed acoustic Mach number $M_a = U_j/c_0$, where c_0 is the sound velocity at ambient temperature, the radiated noise directly depends on the jet temperature. For $M_a < 0.7$, increasing the jet temperature increases the noise; no effect is observed for $M_a = 0.7$ and the noise is reduced with increasing temperature for $M_a > 0.7$. For this last case corresponding to the configurations presented here, the spectral modifications are a decrease of the medium and high frequency levels when temperature rises, while no modifications are visible for the low frequency part of the spectra.

Experimental data reproduced on Fig. 17 exhibit spectral modifications with temperature increase that conform to literature observations. One can nevertheless notice a slight noise increase around 1 kHz at 60 degrees, which was not mentioned in the above-cited published results.

Simulated power spectral densities are illustrated on Fig. 18. Except for very low frequencies, where jet heating reduces the noise levels, calculations reproduce rather well the effect of temperature experimentally described. The decrease of medium and high frequency levels with increasing temperature is especially well observed, as well as the small level increase for the heated jet near 1 kHz at 60 degrees.

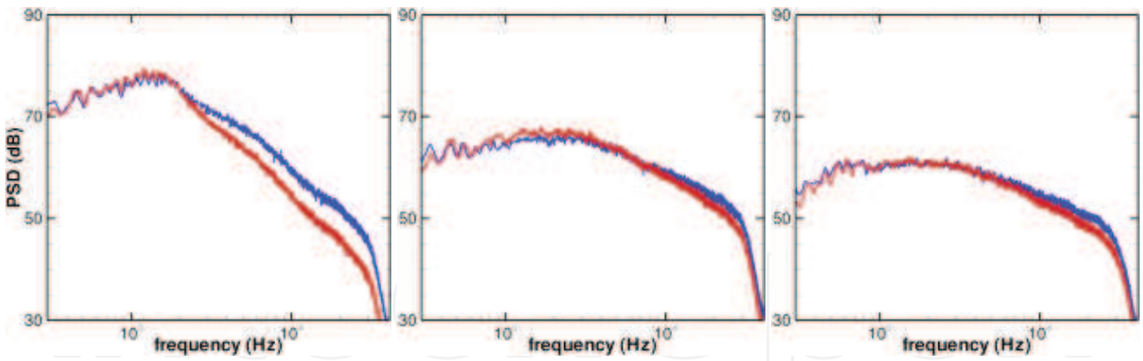

(a) 30 degrees (b) 60 degrees (c) 90 degrees

Fig. 17. Illustration of the temperature effect on power spectral densities for the experimental baseline configurations. – isothermal jet; – heated jet.

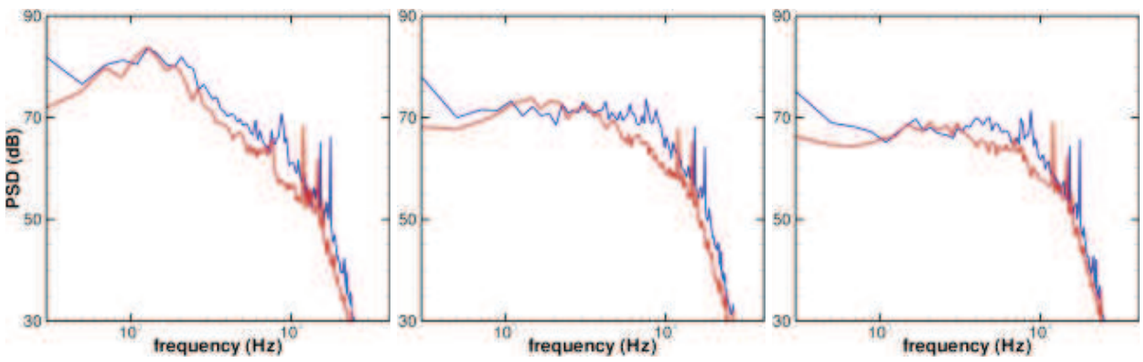

(a) 30 degrees (b) 60 degrees (c) 90 degrees

Fig. 18. Illustration of the temperature effect on power spectral densities for the simulated baseline configurations. – isothermal jet; – heated jet.

Comparing each simulation with the corresponding experiment, see Figs. 19 & 20, one first observes tonal noises in the computations for frequencies above 10 kHz. Those peaks are not observed experimentally and come from the vortex shedding and multiple pairings previously evidenced in §3.1. They are thus a consequence and an illustration of the initially laminar development of the simulated jets. It is coherent with the linear stability analysis presented above; the frequencies of these tonal noises are indeed close to the most unstable shear layer frequency in the vicinity of the jet exhaust, as visible on Fig. 16. These tones are nevertheless not very energetic and do not significantly contribute to the integrated levels.

Simulated PSD also overestimate experiments by about 5 dB, with for instance a maximum level of 84 dB at the peak frequency in both simulations, compared to 79 dB for the measured data. These higher calculated levels can be explained by the overestimation of the turbulent kinetic energy in the jet, as discussed in §3.1. Numerical spectra nevertheless qualitatively well collapse with experiments especially at low angles, for which the frequency of maximum level is particularly very well reproduced. The important levels observed numerically around 5 kHz at 90 degrees, particularly visible for the isothermal jet, are explained by the initially laminar jet, which generates an additional sound source compared to an initially turbulent jet (Bogey & Bailly, 2010).

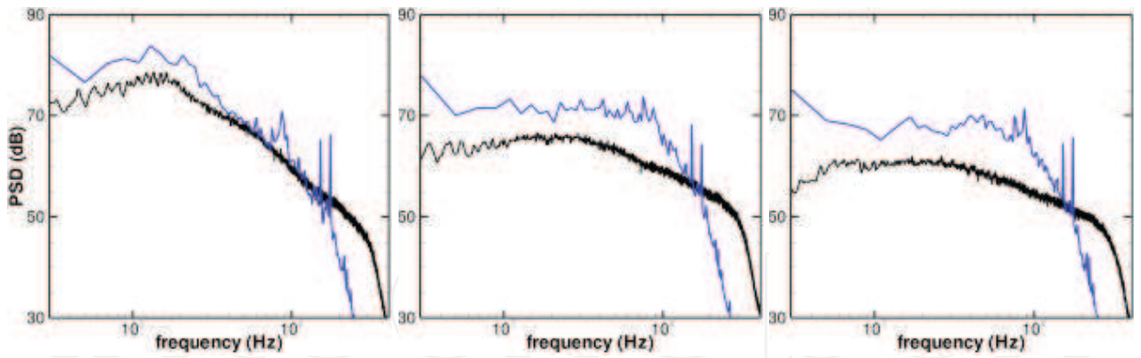

(a) 30 degrees (b) 60 degrees (c) 90 degrees

Fig. 19. Comparison of experimental and computed power spectral densities for the isothermal jet. – experiments; – simulations.

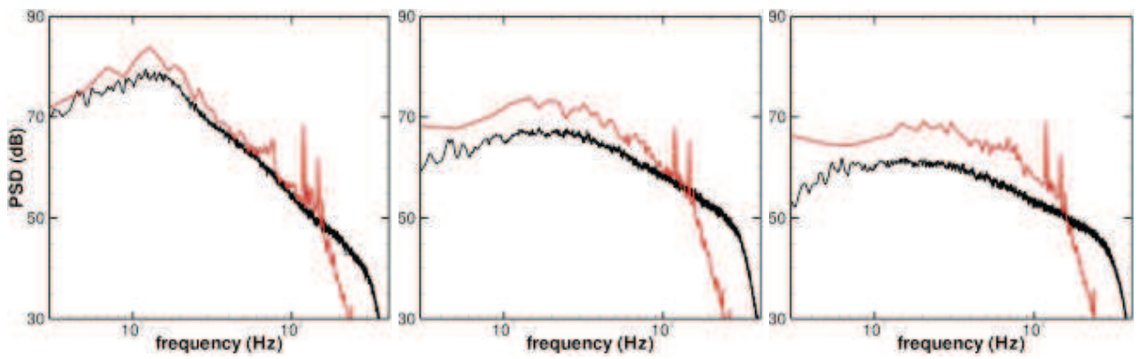

(a) 30 degrees (b) 60 degrees (c) 90 degrees

Fig. 20. Comparison of experimental and computed power spectral densities for the heated jet. – experiments; – simulations.

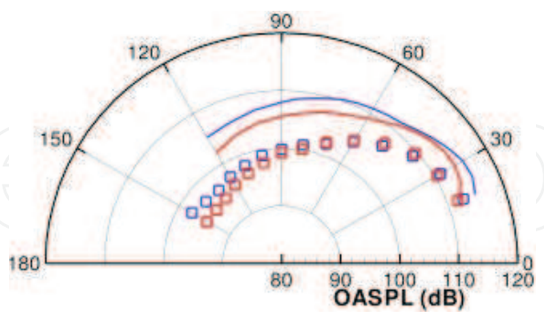

Fig. 21. Experimental and computed integrated levels for isothermal (blue) and heated (red) baseline configurations. □ experiments ; – simulations.

As a consequence of the observations made on PSD, simulated OASPL, represented on Fig. 21, overestimate the measurements at all angles of about 6 dB. Directivity patterns are nevertheless well recovered in the computations, with for instance the maximum level found at about 30 degrees for all configurations. The medium and high frequency levels reduction observed in the spectra for the heated jet lead to lower integrated noise levels for almost all

angles. Near 50 degrees, however, experimental OASPLs are higher for the hot jet and are very close between the two temperatures for the simulations. This difference is caused by the more important noise increase near 1 kHz observed experimentally. To end, the reduction is more pronounced in the simulations with a 2.3 dB difference at 90 degrees, for example, compared to 0.7 dB in the experiments.

The simulated acoustic results obtained for both jets are coherent with the aerodynamic observations made previously. A good qualitative agreement is made with the experiments, the overestimation of the radiated sound being essentially caused by the higher simulated turbulence levels and the initially laminar jet development. The good agreement between experiments and simulations finally illustrates that jet physics and especially the sound sources are correctly reproduced in the simulations for both temperatures and allow the investigation of noise reduction with microjets.

4.2 Continuous microjets

Experimental power spectral densities without and with continuous microjets are reproduced on Figs. 22 & 23 for the isothermal and heated jets, respectively, and integrated levels are visible on Fig. 24. Spectra present high frequency bumps at 60 degrees, caused by reflection on the microphone that is located too close to the acoustically treated ground. Those bumps however occur for levels far below the peak ones and thus do not contaminate the integrated pressure levels. They are moreover high frequency perturbations above the accurately resolved numerical frequencies and do not prevent the relative comparisons of the spectra without and with microjets for energetic levels.

For both temperatures, the noise modifications caused by the microjets are similar to the literature results of Alkislar (Alkislar et al., 2007) and Castelain (Castelain et al., 2008) for isothermal jets, with essentially the most important spectral reduction observed close to the peak frequency and a reduction of the OASPL levels over the entire range of measurement angles caused by the medium frequency noise decrease. The integrated noise reduction of 1.1 dB observed at 90 degrees is besides very close to that of 1.2 dB measured by Castelain et al. on a similar configuration and with the same mass flow rate ratio per microjet $r_m = 6.7 \times 10^{-4}$.

For the two temperatures, simulated spectral modifications caused by the control are similar to the ones observed in the experiments, see Figs 25 & 26. With the exception of the heated jet at fore angles, where low frequency noise is increased by the presence of the microjets, the low frequency parts of the spectra are barely modified while medium frequency levels are reduced by the actuators. The control nevertheless leads to a higher pressure levels reduction in the simulations, with a noise decrease of more than 2 dB at 60 degrees, for instance, compared to a maximum of 1 dB in the measurements. The minimum frequency for which the noise reduction is observed is also higher in the simulations, with numerically a noticeable attenuation for frequencies above several kHz only, while such a reduction is already observed below 1 kHz experimentally.

This reduction of the pressure levels can be related to the decrease of the turbulence fluctuations in the jet detailed in §3.2. The discrepancies observed can be explained by jet initial state at nozzle exit. It can indeed be expected that the control, designed to favour the collapsing of large turbulent structures, is more effective with the coherent structures present in the initially laminar shear layer than in the turbulent shear layer. Noise reduction might thus be overestimated in the simulations compared to the experiments.

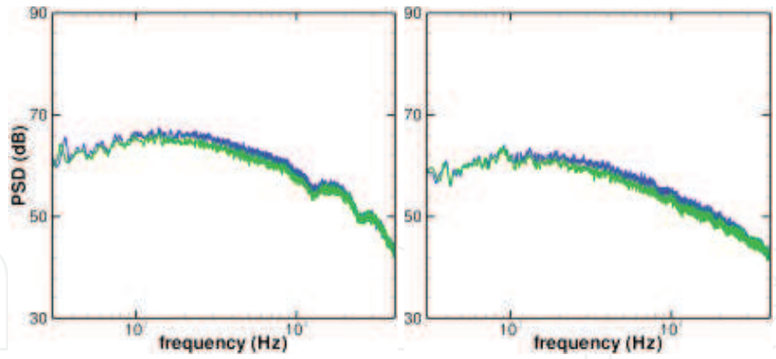

(a) 60 degrees (b) 90 degrees

Fig. 22. Experimental power spectral densities. – baseline; – continuous microjets. Isothermal main jet configuration.

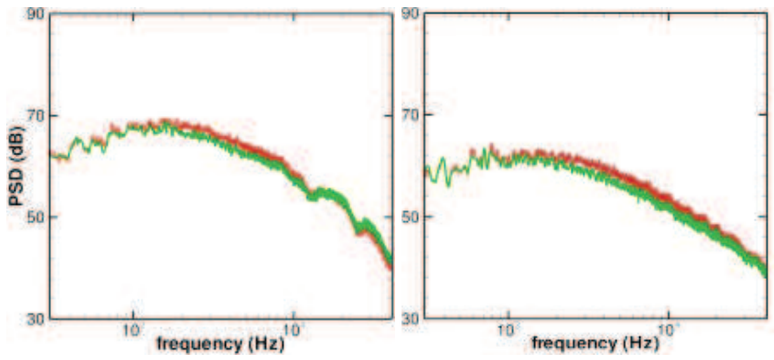

(a) 60 degrees (b) 90 degrees

Fig. 23. Experimental power spectral densities. – baseline; – continuous microjets. Heated main jet configuration.

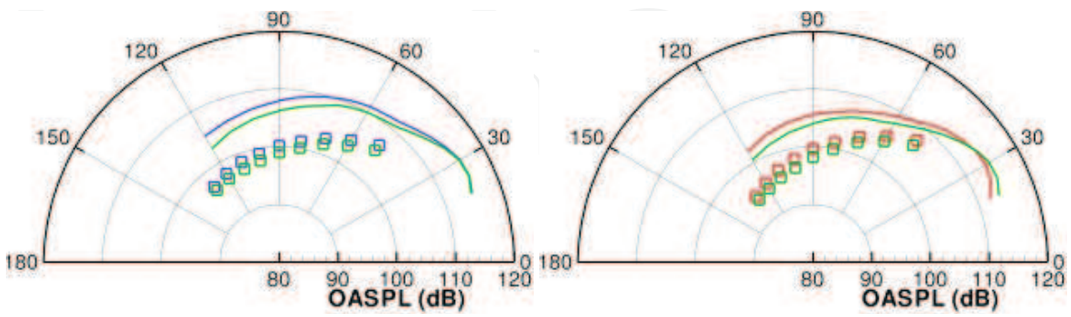

(a) isothermal jet (b) heated jet

Fig. 24. Experimental and computed integrated levels for experimental and simulated (a) isothermal and (b) heated configurations without and with continuous microjets. □ experiments; – simulations. Isothermal baseline in blue, heated baseline in red, continuous microjets in green.

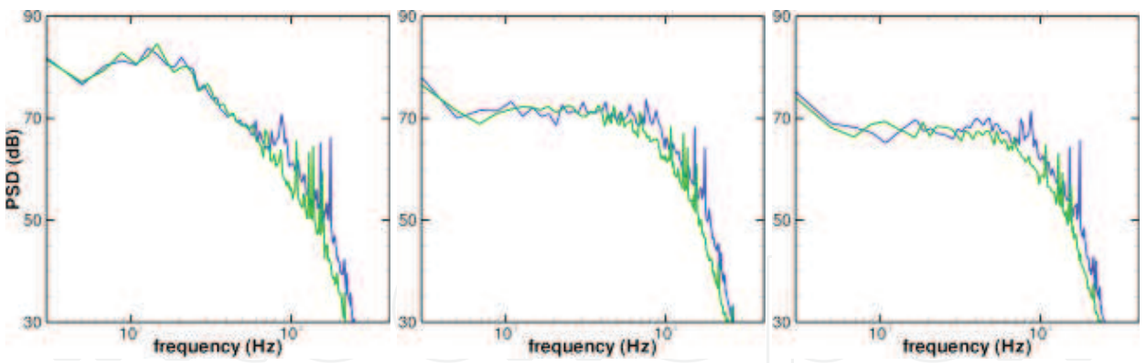

(a) 30 degrees (b) 60 degrees (c) 90 degrees

Fig. 25. Simulated power spectral densities. – baseline; – continuous microjets. Isothermal main jet configuration.

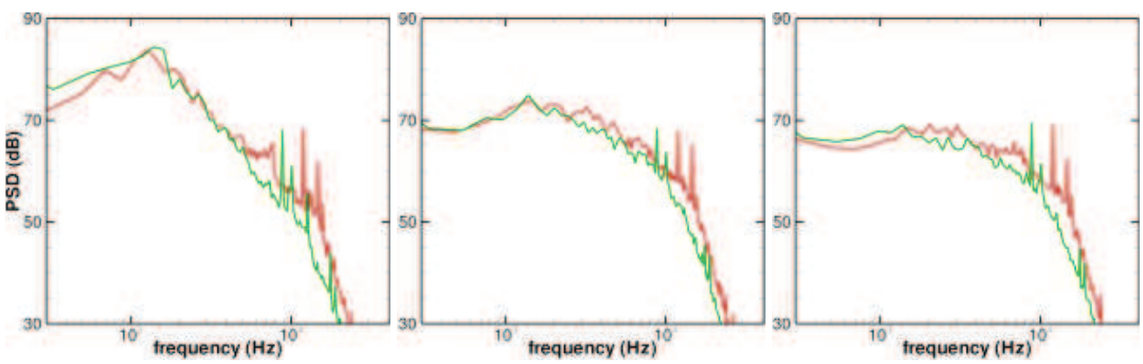

(a) 30 degrees (b) 60 degrees (c) 90 degrees

Fig. 26. Simulated power spectral densities. – baseline; – continuous microjets. Heated main jet configuration.

To end with the spectra modifications, the noise increase at high frequency is not reproduced numerically, because those frequencies and the corresponding noise sources are above the grid cut-off frequency and are thus not properly resolved in the simulations. Not taking into account those high frequency levels is nevertheless not penalizing when computing the integrated pressure levels because those levels are much lower than the most energetic ones and thus have a negligible contribution to the OASPL, as said previously in §2.4.

Integrated pressure levels of the isothermal simulations, visible on Fig. 24 (a), present a noise reduction of 1.1 dB and 1.8 dB, respectively at 60 and 90 degrees. The latter reduction is more important than the experimental one and is a consequence of the larger medium frequency levels reduction with microjets in the simulations, discussed above. Similar OASPL reductions are observed above 50 degrees for the heated jet, with a numerical noise decrease of 1.5 dB at 90 degrees, with comparison to 1.4 dB in the experiments. In this last case, the larger medium frequency noise reduction observed numerically is partly compensated by the low frequency noise increase caused by the control, that finally leads to very close simulated and measured integrated levels.

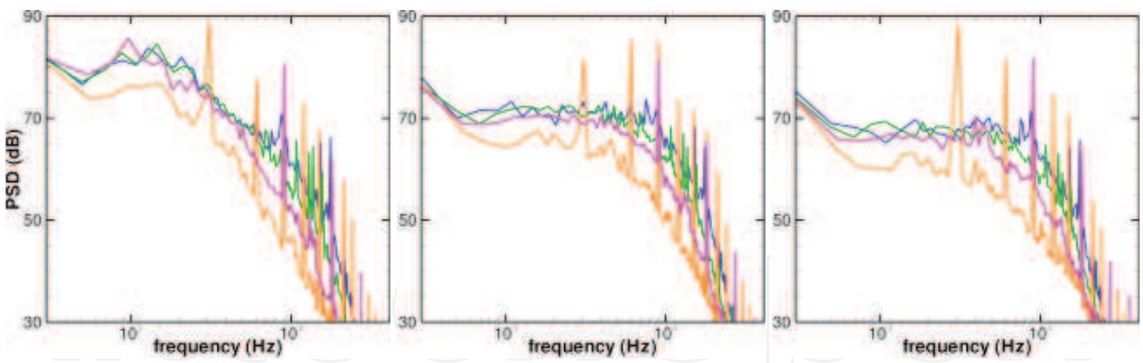

(a) 30 degrees (b) 60 degrees (c) 90 degrees

Fig. 27. Simulated power spectral densities. – baseline; – continuous microjets; – – $f_F = 3$ kHz pulsed microjets; – – $f_F = 9$ kHz pulsed microjets. Isothermal main jet configuration.

No experiments are available close to the jet axis but results from the literature (Alkislar et al., 2007; Castelain et al., 2008) indicate, for isothermal jets, that noise reduction is also expected at fore angles with for instance an attenuation of 0.8 dB at 30 degrees for a configuration similar to the isothermal jet considered in the present study. Such a reduction is not reproduced numerically even if noise levels are reduced above 7 kHz and 4 kHz, respectively for the isothermal and the heated jets. For such angles low frequency noise, around 1 kHz, strongly dominates the spectra and is not reduced by the presence of the microjets. Thus, the medium frequency levels reduction provided by the control is not significant on the integrated levels. This low frequency noise is even increased for the heated jet and leads to a higher OASPL at 20 degrees with microjets, compared to the baseline configuration. A possible reason for experimental and numerical noise discrepancies, jet laminar or turbulent initial state, has already been discussed previously.

4.3 Pulsed microjets

The spectral densities obtained with pulsed control are reproduced on Fig. 27 where are also represented the baseline and continuous microjets configurations spectra. The two principal modifications caused by the pulsed microjets are first the presence of tonal noises at the harmonics of the forcing frequency and second the higher broadband noise reduction compared to continuous control.

The large broadband noise reduction is coherent with the aerodynamic observations and can be linked to the important decrease of the turbulent velocities along the shear layer with the periodic control. Despite the fact that jets developments have been found to be very different with the two forcing frequencies, the broadband noise reduction is similar for the two simulations and corresponds to a large level decrease for almost all frequencies, except for the very low part of the spectra that are not modified by the control. The highest reduction is observed for the $f_F = 3$ kHz forcing with a decrease over 10 dB for a wide frequency range, for which the largest axial turbulent velocity reduction was observed in the shear layer.

The presence of tonal noises is coherent with available literature results and cannot be attributed only to the rough model used for the microjets. Samimy (Samimy et al., 2007a) for instance experimentally observed similar spectral peaks using localized arc filament plasma actuators. Broadband noise modification with the two different forcing frequencies

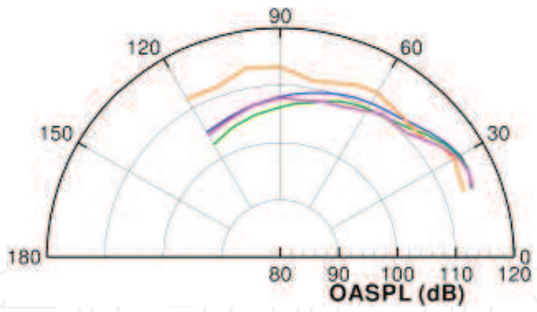

Fig. 28. Simulated integrated pressure levels. – baseline; – continuous microjets; – – $f_F = 3$ kHz pulsed microjets; – – $f_F = 9$ kHz pulsed microjets. Isothermal main jet configuration.

is nevertheless different to that observed by Samimy where a broadband noise increase was observed for the low forcing frequency $f_F = 3$ kHz and a reduction noticed for the high forcing frequency $f_F = 9$ kHz. This difference might come from the different types of actuators used in their measurements and in the present simulations. Experimentally, the control is made through the injection of pure energy while the microjets used numerically correspond to the injection of mass and its convection. It can also be a consequence of the initially laminar state of the simulated shear layer.

If confirmed by further simulations and experiments, those results are of important interest in the use of pulsed control for jet noise reduction. Nevertheless, the gain obtained in the present simulations thanks to the broadband noise reduction is annihilated by the strong contribution of the tonal noises, which finally leads to integrated levels of the same order or greater than that of the baseline configuration for almost all angles, as illustrated on Fig. 28. One must keep in mind that pulsed microjets simulations performed here are a first attempt to illustrate the capacity of the numerical codes to reproduce the actions of such actuators on flow development and noise generation. Flow and noise investigations need to be continued and microjets modelling to be improved to increase the fidelity of the simulations, to evaluate a possible suppression or reduction of the tonal noises or to identify the numerical contribution of the microjets modelling in the far field noise radiation, for instance.

5. Conclusion

Simulations of an isothermal and a heated jet with an acoustic Mach number of 0.9 are presented. Flow and noise modifications caused by continuous microjets are investigated and compared to available experimental data. Noise reduction with pulsed actuators is also investigated for the isothermal configuration.

Simulated baseline configurations present a correct aerodynamic agreement with the experiments. An overestimation of the turbulence in the jet plume is nevertheless observed and can be explained essentially by the different initial state of the shear layer between experiments and simulations. This difference in the initial state, numerically laminar and experimentally turbulent might come from the numerical boundary condition in the nozzle where no flow perturbations are seeded. Far-field pressure spectra are in a good qualitative agreement with the experiments, except for the presence of tonal noises that are a consequence of the jet initially laminar state. Measured directivity patterns are also well recovered in the simulations, with however an overestimation of the absolute levels because of the excessive turbulence in the computed flow.

Flow and noise modifications with increasing temperature are also well reproduced numerically and indicate that the flow physics is well captured in the simulations. Similar conclusions are drawn with the presence of the continuous microjets that notably lead to an axial stretching of the flow fields and a reduction of the medium and high frequency noise of about 1.5 dB at 90 degrees. To end, a drastic turbulence reduction is observed numerically in the shear layer with the use of the pulsed microjets and is accompanied by an important broadband noise reduction in the far field. This noise decrease is nevertheless penalized by important tonal noises at the harmonics of the excitation frequency that makes this control unsuitable for noise reduction as is. Tonal noises have also been observed experimentally for a different type of pulsed actuators and measurements are now required with periodic fluid injection to confirm the promising broadband noise reduction of this type of periodic control.

From all the results presented above, the correct relative effect of the microjets observed numerically on the pressure spectra illustrate the capacity of the simulations to reproduce the action of the control on the flow development, despite the simplified representation of the microjets. Following works will have to focus at first on the simulation of initially turbulent simulated jets to improve flow and noise computation and to reduce discrepancies with the experiments. Improvement of microjets modelling will also be continued, for the pulsed actuators to be more representative of existing experimental devices and also to allow simulations of continuous and periodic controls on larger scale models. The final objective of these future studies is to identify the more promising noise reduction methodology and to help designing optimised experimental devices.

6. Acknowledgments

This work has been conducted within the French project OSCAR (Optimisation de Systèmes de Contrôle Actifs pour la Réduction du bruit de jet) managed by Onera and funded by the FRAE. The authors gratefully acknowledge P. Jordan from Institut PPRIME for providing the JEAN experimental results.

7. References

Alkislar, M. B., Krothapalli, A. & Butler, G. W. (2007). The effect of streamwise vortices on the aeroacoustics of a Mach 0.9 jet, *Journal of Fluid Mechanics* Vol. 578: pp. 139–169.

Andersson, N., Eriksson, L.-E. & Davidson, L. (2005). Large-Eddy Simulation of subsonic turbulent jets and their radiated sound, *AIAA Journal* Vol. 43(No. 9): pp. 1899–1912.

Arakeri, V. H., Krothapalli, A., Siddavaram, V., Alkislar, M. B. & Lourenco, L. M. (2003). On the use of microjets to suppress turbulence in a Mach 0.9 axisymmetric jet, *Journal of Fluid Mechanics* Vol. 490: pp. 75–98.

Biancherin, A. (2003). *Simulation aéroacoustique d'un jet chaud subsonique*, PhD thesis, Université Paris VI.

Bodard, G., Bailly, C. & Vuillot, F. (2009). Matched hybrid approaches to predict jet noise by using Large-Eddy Simulation, *Proceedings of the 15th AIAA/CEAS Aeroacoustics Conference*, number AIAA 2009-3316.

Bodony, D. J. & Lele, S. K. (2005). On using Large-Eddy Simulations for the prediction of noise from cold and heated turbulent jets, *Physics of Fluids* Vol. 17: 085103.

Bogey, C. & Bailly, C. (2006). Computation of a high Reynolds number jet and its radiated noise using Large Eddy Simulation based on explicit filtering, *Computers and Fluids* Vol. 35: pp. 1344–1358.

Bogey, C. & Bailly, C. (2010). Influence of nozzle-exit boundary-layer conditions on the flow and acoustic fields of initially laminar jets, *Journal of Fluid Mechanics* Vol. 663: pp. 507–538.

Bogey, C., Bailly, C. & Juvé, D. (2003). Noise investigation of a high subsonic, moderate Reynolds number jet using a compressible Large Eddy Simulation, *Theoretical and Computational Fluid Dynamics* Vol. 16: pp. 273–297.

Boris, J. P., Grinstein, F. F., Gran, E. S. & Kolbe, R. L. (1992). New insights into Large Eddy Simulation, *Fluid Dynamics Research* Vol. 10: pp. 199–228.

Bridges, J. & Brown, C. A. (2004). Parametric testing of chevrons on single flow hot jets, *Proceedings of the 10th AIAA/CEAS Aeroacoustics Conference*, number AIAA 2004-2824.

Caruana, D., Barricau, P., Hardy, P., Cambronne, J.-P. & Belinger, A. (2009). The "plasma synthetic jet" actuator. Aero-thermodynamic characterization and first flow control applications, *Proceedings of the 47th AIAA Aerospace Sciences Meeting*, number AIAA 2009-1307.

Castelain, T. (2006). *Contrôle de jet par microjets impactants. Mesure de bruit rayonné et analyse aérodynamique*, PhD thesis, École Centrale de Lyon.

Castelain, T., Sunyach, M., Juvé, D. & Béra, J.-C. (2007). Jet noise reduction by impinging microjets: an aerodynamic investigation testing microjet parameters, *Proceedings of the 13th AIAA/CEAS Aeroacoustics Conference*, number AIAA 2007-3419.

Castelain, T., Sunyach, M., Juvé, D. & Béra, J.-C. (2008). Jet noise reduction by impinging microjets: an acoustic investigation testing microjet parameters, *AIAA Journal* Vol. 46(No. 5): pp. 1081–1087.

Courbet, B., Benoit, C., Couaillier, V., Haider, F., Le Pape, M.-C. & Péron, S. (2011). Space discretization methods, *Aerospace Lab* Vol. 2: pp. 1–14.

Dorey, L.-H., Tessé, L., Bertier, N. & Dupoirieux, F. (2010). A strategy for modeling soot formation and radiative transfer in turbulent flames, *Proceedings of the 14th International Heat Transfer Conference*, number IHTC 14-22819.

Dupoirieux, F. & Bertier, N. (2011). The models of turbulent combustion in the CHARME solver of CEDRE, *Aerospace Lab* Vol. 2: pp. 1–7.

Enomoto, S., Yamamoto, K., Yamashita, K., Tanaka, N., Oba, Y. & Oishi, T. (2011). Large-Eddy Simulation of high-subsonic jet flow with microjet injection, *Proceedings of the 17th AIAA/CEAS Aeroacoustics Conference*, number AIAA 2011-2883.

Eschricht, D., Panek, L., Yan, J., Michel, U. & Thiele, F. (2008). Jet noise prediction of a serrated nozzle, *Proceedings of the 14th AIAA/CEAS Aeroacoustics Conference*, number AIAA 2008-2971.

Ffowcs Williams, J. E. & Hawkings, D. L. (1969). Sound generation by turbulence and surfaces in arbitrary motion, *Philosophical Transactions for the Royal Society of London* Vol. A264(No. 1151): pp. 321–342.

Fisher, M. J., Harper-Bourne, M. & Glegg, S. A. L. (1977). Jet engine noise source location: the polar correlation technique, *Journal of Sound and Vibration* Vol. 51(No. 1): pp. 23–54.

Fleury, V., Bailly, C., Jondeau, E., Michard, M. & Juvé, D. (2008). Space-time correlations in two subsonic jets using dual-PIV measurements, *AIAA Journal* Vol. 46(No. 10): pp. 2498–2509.

Freund, J. B. (2001). Noise sources in a low-Reynolds-number turbulent jet at Mach 0.9, *Journal of Fluid Mechanics* Vol. 438: pp. 277–305.

Fureby, C. & Grinstein, F. F. (1999). Monotonically integrated Large Eddy Simulation of free shear flows, *AIAA Journal* Vol. 37(No. 5): pp. 544–556.

Grinstein, F. F. & Fureby, C. (2002). Recent progress on MILES for high Reynolds-number flows, *Journal of Fluids Engineering* Vol. 124(No. 4): pp. 848–861.

Guillou, F. & Chedevergne, F. (2011). Internal turbine blade cooling simulation: advanced models assesment on ribbed configurations, *Proceedings of the 8th Thermal Engineering Joint Conference*, number AJTEC 2011-44295.

Hardy, P., Barricau, P., Belinger, A., Caruana, D., Cambronne, J.-P. & Gleyzes, C. (2010). Plasma synthetic jet for flow control, *Proceedings of the 40th Fluid Dynamics Conference and Exhibit*, number AIAA 2010-5103.

Huet, M., Fayard, B., Rahier, G. & Vuillot, F. (2009). Numerical investigation of the micro-jets efficiency for jet noise reduction, *Proceedings of the 15th AIAA/CEAS Aeroacoustics Conference*, number AIAA 2009-3127.

Husain, Z. D. & Hussain, A. K. M. F. (1979). Axisymmetric mixing layer: Influence of the initial and boundary conditions, *AIAA Journal* Vol. 17: pp. 48–55.

Kastner, J., Kim, J.-H. & Samimy, M. (2008). Toward better understanding of far-field radiated noise mechanisms in a high Reynolds number Mach 0.9 axisymmetric jet, *Proceedings of the 46th AIAA Aerospace Sciences Meeting and Exhibit*, number AIAA 2008-7.

Kearney-Fischer, M., Kim, J.-H. & Samimy, M. (2009a). Control of a high Reynolds number Mach 0.9 heated jet using plasma actuators, *Physics of Fluids* Vol. 21: 095101.

Kearney-Fischer, M., Kim, J.-H. & Samimy, M. (2009b). Noise control of a high Reynolds number Mach 0.9 heated jet using plasma actuators, *Proceedings of the 15th AIAA/CEAS Aeroacoustics Conference*, number AIAA 2009-3188.

Kearney-Fischer, M., Kim, J.-H. & Samimy, M. (2011). A study of Mach wave radiation in an axisymmetric jet using active control, *Proceedings of the 17th AIAA/CEAS Aeroacoustics Conference*, number AIAA 2011-2834.

Kim, J.-H., Kastner, J. & Samimy, M. (2009). Active control of a high Reynolds number Mach 0.9 axisymmetric jet, *AIAA Journal* Vol. 47(No. 1): pp. 116–128.

Krothapalli, A., Venkatakrishnan, L., Lourenco, L., Greska, B. & Elavarasan, R. (2003). Turbulence and noise suppression of a high-speed jet by water injection, *Journal of Fluid Mechanics* Vol. 491: pp. 131–159.

Laufer, J., Schlinker, R. & Kaplan, R. E. (1976). Experiments on supersonic jet noise, *AIAA Journal* Vol. 14(No. 4): pp. 489–497.

Laurendeau, E., Jordan, P., Bonnet, J.-P., Delville, J., Parnaudeau, P. & Lamballais, E. (2008). Subsonic jet noise reduction by fluidic control: The interaction region and the global effect, *Physics of Fluids* Vol. 20: 101519.

Lew, P.-T., A.Najafi-Yazdi & L.Mongeau (2010). Unsteady numerical simulation of a round jet with impinging microjets for noise suppression, *Proceedings of the 48th AIAA Aerospace Sciences Meeting*, number AIAA 2010-18.

Lighthill, M. J. (1952). On sound generated aerodynamically, part I: General theory, *Proceedings of the Royal Society of London* Vol. A221(No. 1107): pp. 564–587.

Lyrintzis, A. S. (1994). Review: the use of Kirchhoff's method in computational aeroacoustics, *Journal of Fluids Engineering* Vol.(No. 4): pp. 665–676.

Michalke, A. (1965). On spatially growing disturbances in an inviscid shear layer, *Journal of Fluid Mechanics* Vol. 23: pp. 521–544.

Muller, F. (2006). *Simulation de jets propulsifs : application à l'identification des mécanismes générateurs de bruit*, PhD thesis, Université Paris VI.

Muller, F., Vuillot, F., Rahier, G., Casalis, G. & Piot, E. (2006). Experimental and numerical investigation of the near field pressure of a high subsonic hot jet, *Proceedings of the 12th AIAA/CEAS Aeroacoustics Conference*, number AIAA 2006-2535.

Najafi-Yazdi, A., Lew, P.-T. & Mongeau, L. (2011). Large Eddy Simulation of jet noise suppression by impinging microjets, *Proceedings of the 17th AIAA/CEAS Aeroacoustics Conference*, number AIAA 2011-2748.

Nesbitt, E. & Young, R. (2008). Forward flight effects on chevron noise reduction, *Proceedings of the 14th AIAA/CEAS Aeroacoustics Conference*, number AIAA 2008-3065.

Perez, G., Prieur, J., Rahier, G. & Vuillot, F. (2007). Theoretical and numerical discussion on volume integral methods for jet noise prediction, *Proceedings of the 13th AIAA/CEAS Aeroacoustics Conference*, number AIAA 2007-3593.

Ragaller, P. A., Annaswamy, A. M., Greska, B. & Krothapalli, A. (2009). Supersonic jet noise reduction via pulsed microjet injection, *Proceedings of the 15th AIAA/CEAS Aeroacoustics Conference*, number AIAA 2009-3224.

Rahier, G., Prieur, J., Vuillot, F., Lupoglazoff, N. & Biancherin, A. (2004). Investigation of integral surface formulations for acoustic post-processing of unsteady aerodynamic jet simulations, *Aerospace Science and Technology* Vol. 8: pp. 453–467.

Rife, M. E. & Page, G. J. (2011). Large Eddy Simulation of high Reynolds number jets with microjet injection, *Proceedings of the 17th AIAA/CEAS Aeroacoustics Conference*, number AIAA 2011-2882.

Samimy, M., Kim, J.-H., Kastner, J., Adamovich, I. & Utkin, Y. (2007a). Active control of a Mach 0.9 jet for noise mitigation using plasma actuators, *AIAA Journal* Vol. 45(No. 4): pp. 890–901.

Samimy, M., Kim, J.-H., Kastner, J., Adamovich, I. & Utkin, Y. (2007b). Active control of high-speed and high-Reynolds-number jets using plasma actuators, *Journal of Fluid Mechanics* Vol. 578: pp. 305–330.

Shur, M. L., Spalart, P. R. & Strelets, M. K. (2011). LES-based evaluation of a microjet noise reduction concept in static and flight conditions, *Journal of Sound and Vibration* Vol. 330: pp. 4083–4097.

Smagorinsky, J. (1963). General circulation experiments with the primitive equations, *Monthly Weather Review* Vol. 91(No. 3): pp. 99–164.

Tam, C. K. W., Viswanathan, K., Ahuja, K. K. & Panda, J. (2008). The sources of jet noise: experimental evidence, *Journal of Fluid Mechanics* Vol. 615: pp. 253–292.

Tanna, H. (1977). An experimental study of jet noise, part I: Turbulent mixing noise; part II: Shock associated noise, *Journal of Sound and Vibration* Vol. 50(No. 3): pp. 405–444.

Tanna, H., Dean, P. & Fisher, M. (1975). The influence of the temperature on shock-free supersonic jet noise, *Journal of Sound and Vibration* Vol. 39(No. 4): pp. 429–460.

Uzun, A. & Hussaini, M. Y. (2009). Simulation of noise generation in near-nozzle region of a chevron nozzle jet, *AIAA Journal* Vol. 47(No. 8): pp. 1793–1810.

Viswanathan, K. (2004). Aeroacoustics of hot jets, *Journal of Fluid Mechanics* Vol. 516: pp. 39–82.

Vuillot, F., Lupoglazoff, N. & Huet, M. (2011). Effect of chevrons on double stream jet noise from hybrid CAA computations, *Proceedings of the 49th AIAA Aerospace Sciences Meeting*, number AIAA 2011-1154.

Xia, H., Tucker, P. G. & Eastwood, S. (2008). Towards jet flow LES of conceptual nozzles for acoustic predictions, *Proceedings of the 46th AIAA Aerospace Sciences Meeting and Exhibit*, number AIAA 2008-10.

Yan, J., Tawackolian, K., Michel, U. & Thiele, F. (2007). Computation of jet noise using a hybrid approach, *Proceedings of the 13th AIAA/CEAS Aeroacoustics Conference*, number AIAA 2007-3621.

Zaman, K. B. M. Q. (1985). Far-field noise of a subsonic jet under controlled excitation, *Journal of Fluid Mechanics* Vol. 152: pp. 83–111.

Zaman, K. B. M. Q. (2010). Subsonic jet noise reduction by microjets - a parametric study, *International Journal of Aeroacoustics* Vol. 9(No. 6): pp. 705–732.

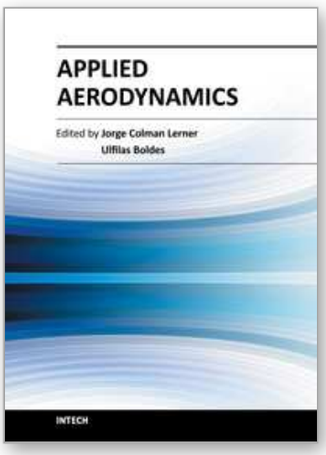

Applied Aerodynamics

Edited by Dr. Jorge Colman Lerner

ISBN 978-953-51-0611-1

Hard cover, 192 pages

Publisher InTech

Published online 11, May, 2012

Published in print edition May, 2012

Aerodynamics, from a modern point of view, is a branch of physics that study physical laws and their applications, regarding the displacement of a body into a fluid, such concept could be applied to any body moving in a fluid at rest or any fluid moving around a body at rest. This Book covers a small part of the numerous cases of stationary and non stationary aerodynamics; wave generation and propagation; wind energy; flow control techniques and, also, sports aerodynamics. It's not an undergraduate text but is thought to be useful for those teachers and/or researchers which work in the several branches of applied aerodynamics and/or applied fluid dynamics, from experiments procedures to computational methods.

InTech Europe
University Campus STeP Ri
Slavka Krautzeka 83/A
51000 Rijeka, Croatia
Phone: +385 (51) 770 447
Fax: +385 (51) 686 166
www.intechopen.com

InTech China
Unit 405, Office Block, Hotel Equatorial Shanghai
No.65, Yan An Road (West), Shanghai, 200040, China
中国上海市延安西路65号上海国际贵都大饭店办公楼405单元
Phone: +86-21-62489820
Fax: +86-21-62489821

IntechOpen